

SPITZER AND NEAR-INFRARED OBSERVATIONS OF A NEW BI-POLAR PROTOSTELLAR OUTFLOW IN THE ROSETTE MOLECULAR CLOUD

JASON E. YBARRA¹ AND ELIZABETH A. LADA

Department of Astronomy, University of Florida, Gainesville, FL 32605

ZOLTAN BALOG

Max-Planck-Institut für Astronomie, Heidelberg, Germany

SCOTT W. FLEMING¹

Department of Astronomy, University of Florida, Gainesville, FL 32605

RANDY L. PHELPS²

National Science Foundation, Office of Integrative Activities, Arlington, VA 22230

Accepted for publication in the Astrophysical Journal

ABSTRACT

We present and discuss *Spitzer* and near-infrared H₂ observations of a new bi-polar protostellar outflow in the Rosette Molecular Cloud. The outflow is seen in all four IRAC bands and partially as diffuse emission in the MIPS 24 μm band. An embedded MIPS 24 μm source bisects the outflow and appears to be the driving source. This source is coincident with a dark patch seen in absorption in the 8 μm IRAC image. *Spitzer* IRAC color analysis of the shocked emission was performed from which thermal and column density maps of the outflow were constructed. Narrow-band near-infrared (NIR) images of the flow reveal H₂ emission features coincident with the high temperature regions of the outflow. This outflow has now been given the designation MHO 1321 due to the detection of NIR H₂ features. We use these data and maps to probe the physical conditions and structure of the flow.

Subject headings: ISM: jets and outflows — ISM: individual objects (MHO 1321) — methods: data analysis

1. INTRODUCTION

Outflows and jets from young stellar objects (YSOs) accompany the early stages of star formation. Outflows can manifest themselves as jets and knots of shocked material visible at optical and near-infrared wavelengths and also molecular emission observable at longer wavelengths. The outflowing material plays a role in removing the excess angular momentum from the YSOs allowing them to evolve into stars. Outflows are able to trace the history of mass loss and accretion of their driving sources. Studying the structure and properties of these flows may provide clues to understanding the connection between jets and the associated wide angle molecular flows (Reipurth & Bally 2001). Additionally, this outflowing material interacts with its surroundings and may affect its environment, possibly regulating further star formation and cluster evolution. The energy and momentum inputted by outflows may disrupt the surrounding ambient gas, contribute to the turbulence in the cloud, and affect chemical processes (Bally 2007).

jybarra@astro.ufl.edu

¹ Visiting astronomer, Cerro Tololo Inter-American Observatory, National Optical Astronomy Observatory, which are operated by the Association of Universities for Research in Astronomy, under contract with the National Science Foundation.

² This material is based on work supported by the National Science Foundation. Any opinion, findings, and conclusion or recommendations expressed in this material are those of the author and do not necessarily reflect the views of the National Science Foundation

Ybarra & Lada (2009) developed a technique to study the thermal structure of shocked H₂ gas using color analysis of observations from the *Spitzer* InfraRed Array Camera (IRAC). Given the vast amount of *Spitzer* data available, this technique can be used to survey large regions and simultaneously find and analyze shocked emission. The IRAC color analysis enables the construction of temperature maps of the shocked gas which may in turn be used to probe the interaction of outflow with its surroundings. These maps may also be used to compare the properties of outflow with those of simulations allowing a better understanding of the physics involved and estimating the energy and momentum inputted by outflows into their environment.

The Rosette Molecular Cloud (RMC) is a star forming region located at a distance of 1.6 kpc. Near-infrared imaging studies have revealed nine embedded clusters across the cloud (Phelps & Lada 1997; Román-Zúñiga et al. 2008). Outflow activity in the cloud has been revealed through the [S II] narrowband imaging survey of Ybarra & Phelps (2004) and the ¹²CO survey of Dent et al. (2009). In an analysis of the *Spitzer* IRAC images of the Rosette Molecular Cloud, we have discovered a structure with the morphology of a bipolar outflow that is visible in the images from all four IRAC bands. This structure can be seen in the images published by Poulton et al. (2008) although it is not discussed in their paper.

In this study we analyze the outflow using near infrared

(NIR) narrowband imaging of the flow to confirm the presence of shocked gas inferred from analysis of the the IRAC images. We improve the IRAC color analysis of Ybarra & Lada (2009) and use it to create temperature and column density maps of the outflow. Using both the NIR and IRAC data, we probe the physical conditions and structure of the outflow.

2. OBSERVATIONS AND DATA REDUCTION

2.1. *Spitzer IRAC and MIPS data reduction*

We used MIPS $24\mu\text{m}$ and IRAC $3.6\text{--}8.0\mu\text{m}$ data from program 3391 (PI: Bonnel) available in the *Spitzer* archive. The IRAC frames were processed using the Spitzer Science Center (SSC) IRAC Pipeline v14.0, and mosaics were created from the basic calibrated data (BCD) frames using a custom IDL program (see Gutermuth et al. (2008) for details). The MIPS frames were processed using the MIPS Data Analysis Tool (Gordon et al. 2005).

2.2. *Near-Infrared H_2 observations and data reduction*

Near-Infrared, narrow-band observations of the outflow were obtained with the Infrared Side Port-Imager (ISPI) on the Blanco 4 meter telescope at the Cerro Tololo Inter-American Observatory (CTIO). ISPI employs a 2048×2048 HgCdTe Hawaii-2 array with a 10.25×10.25 arcmin field of view and a plate scale of $\sim 0.305''$ pixel $^{-1}$. The outflow was imaged using the H_2 1–0 S(2) $2.034\mu\text{m}$ filter ($\lambda_c = 2.0336\mu\text{m}$, $\Delta\lambda/\lambda = .007$), H_2 1–0 S(1) $2.122\mu\text{m}$ filter ($\lambda_c = 2.1262\mu\text{m}$, $\Delta\lambda/\lambda = .01$), and K_{cont} filter centered at $2.1462\mu\text{m}$. The telescope was dithered with a 20 point dither pattern with a integration time of 60s at each dither position. The images were taken on the nights of 2008 December 17 and 2008 December 19 with total integration time of 40 minutes in each filter.

The raw images were flat fielded, corrected for bad pixels, and linearized using the task `osiris` from the CTIO Infrared Reduction package. For each image, a sky frame was created by median combining the dithered images closest in time to the image. The IRAF tasks `msctpeak` and `mscimage`, which are part of the IRAF Mosaic Data Reduction Package, `mscred`, were used to correct the images for geometric distortions. The high order polynomial distortion terms were calculated with `msctpeak` using the 2MASS Point Source Catalog as the reference catalog and the distortion correction was applied with `mscimage`. The corrected images were aligned and then combined to form the final science images.

3. RESULTS AND ANALYSIS

Figure 1 shows the outflow in all four IRAC bands. The outflow appears as patchy regions of diffuse emission with an overall structure that is elongated and collimated in the E-W direction. Figure 2 shows the narrowband near-infrared emission images of the outflow. The NIR H_2 knots coincide with the diffuse emission seen in the IRAC images. The NIR H_2 images confirm the presence of shocked gas and the interpretation that this structure is an outflow. The eastern end appears to truncate at a bow shock. Slightly west of the bow shock, the H_2 images reveal a small scale chaotic structure followed by a more linear chain of knots. The western end of the outflow

Table 1
Positions and flux estimates for the NIR H_2 knots of MHO 1321

Knot	R.A. (J2000)	Dec (J2000)	H_2 1–0 S(2)	H_2 1–0 S(1)
a	06:35:20.08	+03:56:37.9	4.1±2.0	7.6±2.2
b	06:35:21.64	+03:56:28.8	2.2±1.4	8.9±2.2
c	06:35:21.82	+03:56:32.3	3.9±1.9	12.5±2.4
d	06:35:21.85	+03:56:27.6	4.2±1.8	15.6±2.8
e	06:35:22.19	+03:56:29.5	2.2±1.7	10.1±2.4
f	06:35:22.70	+03:56:33.2	2.0±1.6	4.9±2.1
g	06:35:22.90	+03:56:28.7	15.5±3.8	52.4±5.8
h	06:35:23.21	+03:56:17.3	1.2±1.5	3.3±1.8
i	06:35:23.77	+03:56:24.1	1.8±1.6	5.2±1.9
j	06:35:24.33	+03:56:21.6	4.7±2.2	20.8±3.4
k	06:35:24.61	+03:56:20.7	2.5±1.6	10.4±2.4
l	06:35:25.26	+03:56:21.4	2.4±1.6	8.3±2.1
m	06:35:25.46	+03:56:21.6	1.5±1.3	4.3±1.8
n	06:35:26.13	+03:56:20.9	2.0±1.7	8.6±2.5
o	06:35:26.57	+03:56:23.5	1.4±1.4	3.3±1.6
p	06:35:27.90	+03:56:18.3	3.1±1.9	11.8±2.6
q	06:35:28.56	+03:56:25.7	3.0±2.0	10.8±2.6
r	06:35:29.02	+03:56:14.2	12.8±3.4	42.3±5.0
s	06:35:29.18	+03:56:18.6	2.1±1.6	6.9±2.0
t	06:35:31.16	+03:56:15.8	1.6±1.5	4.3±1.8
u	06:35:33.64	+03:56:16.6	3.0±1.7	11.3±2.6
v	06:35:33.85	+03:56:18.9	2.8±1.9	7.9±2.1
w	06:35:34.04	+03:56:20.5	2.0±1.5	5.1±2.0

Note. — Flux is in units of 10^{-18} W m^{-2} . Aperture radius used is 7 pixels. Flux uncertainty includes calibration uncertainty

appears slightly deflected northward followed by a bright knot (g) and then a complex structure of smaller knots.

The NIR images were flux calibrated to the 2MASS Ks band by determining the magnitude difference between the 2MASS Ks band catalog values and the ISPI image magnitudes for stars in common. The zero point flux in each NIR image after calibration is then the filter bandwidth multiplied by the 2MASS Ks-band zero point flux density. This results in a relation between the counts sec^{-1} in each filter image and the flux in W cm^{-2} . The narrow band continuum K_c images were scaled and subsequently subtracted from the H_2 line images. Figures 2c and 2d show the continuum subtracted H_2 1–0 S(1) $2.122\mu\text{m}$ and H_2 1–0 S(2) $2.034\mu\text{m}$ line images. The quality of the subtraction is good although there are some subtraction residuals from the brightest stars present in the subtracted images due to differences in wavelength and PSF combined with changing atmospheric conditions.

Based on the observation, this outflow has been given the designation MHO 1321 in the Catalogue of Molecular Hydrogen Emission-Line Objects (MHOs) in Outflows from Young Stars³ (Davis et al. 2009). The fluxes of the individual H_2 knots comprising this outflow were determined using a circular aperture on the continuum subtracted images. Table 1 lists the NIR fluxes of the H_2 emission knots. The flux uncertainty is composed of the rms background, poisson noise, and uncertainty from the flux calibration.

3.1. *IRAC color space of shocked gas*

In order to study the structure of the shocked gas, we applied the IRAC color analysis method developed by Ybarra & Lada (2009). We improved the color analysis method by including the effects of CO $\nu=1\text{--}0$ band emission in the total emission of the shocked

³ MHO catalogue is hosted by the Joint Astronomy Centre, Hawaii. <http://www.jach.hawaii.edu/UKIRT/MHCat/>

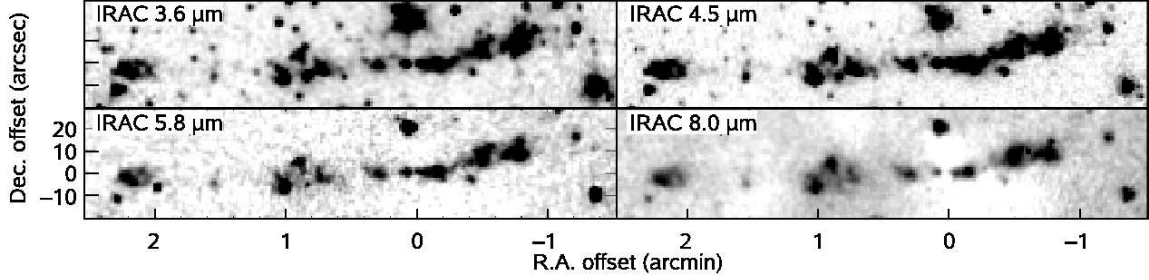


Figure 1. Spitzer IRAC images of the outflow. The origin is set at $(\alpha, \delta)(J2000) = (06^{\text{h}}35^{\text{m}}25^{\text{s}}.0, +03^{\circ}56'21'')$

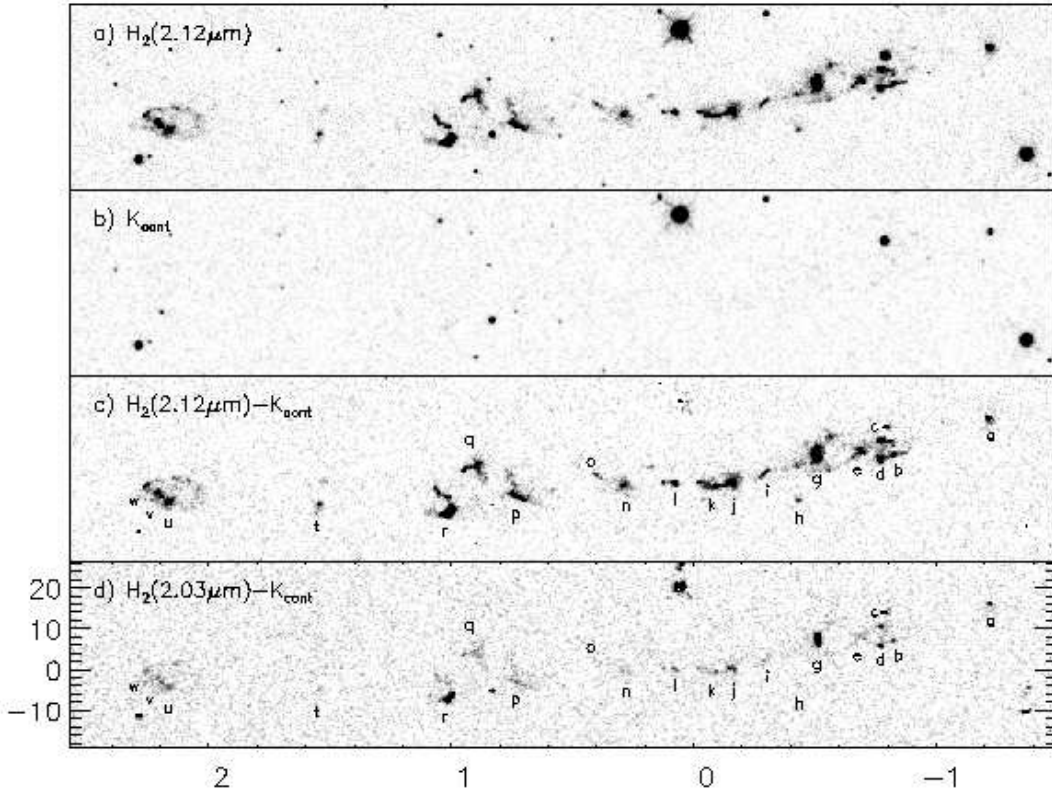


Figure 2. Near-infrared images of the outflow: a) H_2 1–0 S(1) 2.122 μm line, b) K_{cont} , c) continuum subtracted H_2 1–0 S(1) 2.122 μm , d) continuum subtracted H_2 1–0 S(2) 2.034 μm . The horizontal scale is in arcminutes and the vertical scale is in arcseconds. The origin is set at $(\alpha, \delta)(J2000) = (06^{\text{h}}35^{\text{m}}25^{\text{s}}.0, +03^{\circ}56'21'')$

gas. The distribution of the population of pure rotational levels of CO due to collisional excitation with H_2 , H, and He was calculated using the rate coefficients of Draine & Roberge (1984). We employed the method of González-Alfonso et al. (2002) to calculate the relative rotational population for the CO $\nu=1$ vibrational level. The Einstein A-values for the CO $\nu=1-0$ rovibrational transitions were obtained using the oscillator strengths of Hure & Roueff (1993). In our calculations, we set $n_{\text{H}} = n(\text{H}) + 2n(\text{H}_2)$, $n(\text{He})/n_{\text{H}} = 0.1$ and $n(\text{CO})/n_{\text{H}} = 7 \times 10^{-5}$. The fraction of atomic to molecular hydrogen was estimated by considering the rate of collisional dissociation by H atoms, $R_d = 1.0 \times 10^{-10} \exp(-52000/T) \text{ cm}^3 \text{ s}^{-1}$ (Le Bourlot et al. 2002) and the rate of formation on grains, $R_f = 3.8 \times 10^{-17} T^{-1.5} \text{ cm}^3 \text{ s}^{-1}$, derived from

Hollenbach & McKee (1979) with the cooling rates for H_2 and H_2O (Le Bourlot et al. 1999, 2002).

Figure 3 shows the location of shocked gas in IRAC [3.6]–[4.5] versus [4.5]–[5.8] color space for maximum shock temperature of $T_{\text{max}} = 6 \times 10^3 \text{ K}$ for gas temperatures $T = 1500 - 5000 \text{ K}$ and densities $n_{\text{H}} = 10^5 - 10^7 \text{ cm}^{-3}$. The square brackets refer to IRAC magnitudes. The post-shock fraction of atomic hydrogen was found to be $n(\text{H})/n_{\text{H}} \sim 1 - 4 \times 10^{-3}$ which is consistent with simulations of non-dissociative C-shocks (Wilgenbus et al. 2000). In the simulations by Wilgenbus et al. (2000) it was found that the atomic fraction is relatively constant over a wide range of maximum temperatures. Therefore we will assume our color space to be representative of non-dissociative C-shocks in general. The location of the shocked emission in IRAC color space depends on the

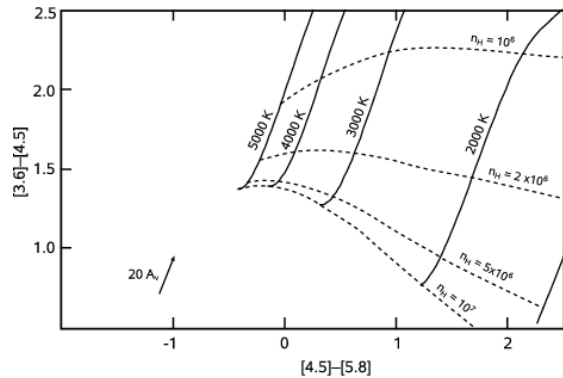


Figure 3. IRAC color-color plot indicating the region occupied by shocked gas composed of H_2 and CO for $T_{\text{max}} = 6 \times 10^3$ K

gas density, fraction of atomic hydrogen, and the kinetic temperature of the gas. The $[4.5]-[5.8]$ color is strongly dependent on temperature, while the $[3.6]-[4.5]$ color has a strong dependence on the atomic hydrogen density. At high densities, the dependence on density decreases as the H_2 gas moves toward local thermal equilibrium (LTE). The slope of the reddening vector is similar to the approximate slope of the constant temperature lines. Thus temperature maps of high extinction regions remain accurate even if the extinction cannot be accounted for. However, unless extinction can be corrected for, accurate density information may not be attainable.

We fit an analytic form to the relationship between color and temperature for the non-dissociative case,

$$T_3 = 4.19 - 0.97([3.6]-[4.5]) - 2.11([4.5]-[5.8]) + 0.59([3.6]-[4.5])^2 + 0.50([4.5]-[5.8])^2$$

where $T_3 = T/10^3$ in the color space defined by $2.0 > [3.6]-[4.5] > -0.21([4.5]-[5.8]) + 1.5$, and $-0.2 < [4.5]-[5.8] < 2.0$. The difference between the analytic fit and the calculated temperature-color relation over the defined range is less than 10%. Additionally, one can use the flux in the $3.6 \mu\text{m}$ image to estimate the column density of the shocked H_2 . Using our calculations we fit the following analytic form to the relationship between column density, IRAC $3.6 \mu\text{m}$ flux density, and temperature,

$$\log(N_{\text{H}_2}/F_{3.6}) = 23.11 - 3.40T_3 + 0.742T_3^2 - 0.0589T_3^3 - 0.071n_6 + 0.012n_6T_3$$

where N_{H_2} is the column density of shocked H_2 in cm^{-2} , $F_{3.6}$ is the IRAC $3.6 \mu\text{m}$ band flux density in units of MJy sr^{-1} , and $n_6 = n_{\text{H}}/10^6$ for $1.5 < T_3 < 5.0$ and $2 < n_6 < 10$.

In order to investigate the color space of dissociative J-type shocks we simulated the gas properties of a dissociative shock by setting the maximum temperature of the gas to $T_{\text{max}} = 1 \times 10^4$ K. Our calculations show significant dissociation of H_2 with increasing density. Figure 4 shows the IRAC color space for dissociatively shocked gas. As the molecular hydrogen gets dissociated, emission from the $\text{CO } \nu=1-0$ band begins to dominate the $4.5 \mu\text{m}$ IRAC channel.

The relationships between temperature, density and color are different for the case of the non-dissociative shock and the case of the dissociative shock. There is

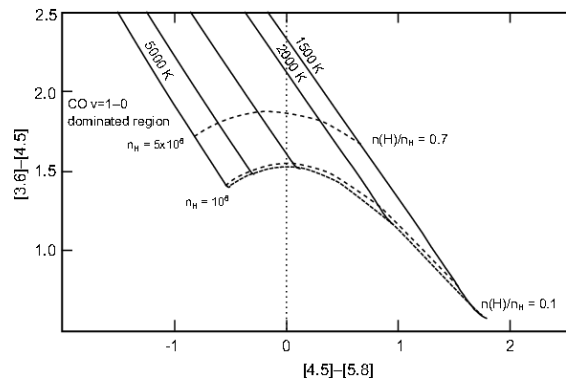


Figure 4. IRAC color-color plot indicating the region occupied by dissociatively shocked gas composed of H_2 and CO

some degeneracy at the low density and low dissociation region of color space for the dissociative shock and at the high density non-dissociative shock region. These two models meet in a region of color space defined by H_2 gas in LTE. Although there is degeneracy, we expect the distribution in color space for the dissociative shock to primarily lie at $[4.5]-[5.8] < 0$. Thus we define the domain of the dissociative shocked gas in color space to be $[4.5]-[5.8] < 0$ and $[3.6]-[4.5] > 1.5$, whereas we define the color domain of non-dissociative gas to lie primarily at $[4.5]-[5.8] > 0$. By analyzing the color distribution of an outflow, it may be possible to distinguish between the cases. A pixel density distribution, produced from binning the colors of each pixel in the the outflow, can reveal the nature of the outflow by showing where most of the pixels lie in color space.

It should be noted that the IRAC color analysis assumes dust and PAH emission is negligible. In order to prevent dust emission from affecting the color analysis, the $8 \mu\text{m}$ IRAC color is not used as there is evidence in some shocks of continuum dust emission within that wavelength range covered by the $8 \mu\text{m}$ channel (eg. Smith et al. 2006). Additionally, PAHs are very likely destroyed in shocks. In a recent study, Micelotta et al. (2010) show that strong shocks can destroy PAHs or severely denature them.

3.2. IRAC color analysis of MHO 1321

The IRAC $8 \mu\text{m}$ image of the outflow region reveals patches of absorption against the diffuse background (Figure 1). Of particular interest is a dark patch seen in absorption that bisects the outflow. We created an extinction map from the $8 \mu\text{m}$ data using a small scale median filter assuming a uniform background. We applied this extinction map to the images of the outflow region using the mid-infrared reddening law (KP, v5.0) of Chapman et al. (2009). However, this is not able to account for the total extinction in the line of sight toward the outflow. Nonetheless, the temperature-color relation is insensitive to extinction for non-dissociative shocks. We estimate the background using a ring median filter and subsequently remove this background from the IRAC $3.6 \mu\text{m}$, $4.5 \mu\text{m}$, and $5.8 \mu\text{m}$ images. A ring median filter is a median filter from which only the pixels within an annulus are used in calculating the median (Secker 1995). The scale of this filter needs to be larger than the scale of the shocked emission otherwise the background will be overestimated, yet small enough to account for the large

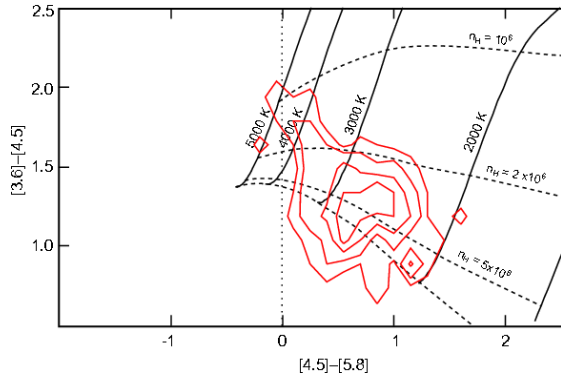


Figure 5. Contours indicate the pixel density in IRAC color space of the outflow knots. The distribution of pixels and the lack of pixels in the CO dominated region indicate non-dissociative shocks.

scale background fluctuations. The images were shifted and registered with each other and then IRAC colors at each pixel location were determined. Figure 5 shows the pixel density in IRAC color space for the knots of the outflow. Due to the lack of pixels whose colors are in or near the CO dominated region and our criteria above for non-dissociative shocks, we conclude that this shock is mostly non-dissociative and we can therefore estimate the thermal structure based on color analysis. We compared the colors to those of non-dissociative shocked gas with the cutoff $[4.5]-[5.8] \leq 1.5$. A thermal map was created by estimating the gas temperature based on the location of the pixels in color space. Figure 6 shows the thermal map of the outflow.

We find that most of the NIR H_2 knots are spatially coincident with the high temperature regions of the flow. However, knots a and v do not have a corresponding IRAC derived temperature. The NIR images reveal stars in the line of sight for these knots which add to the emission and prevents IRAC color analysis from deriving temperatures. Seven of the knots have estimated temperatures greater or equal to 3×10^3 K. By combining the NIR infrared and temperature data it is possible to estimate the extinction towards the brightest knots. For this we used the extinction cross-sections of Weingartner & Draine (2001). The median extinction to the knots is $A_v = 27$. The knots j and k in the vicinity of the dark clump have higher extinction compared to the rest of the knots. We use the median extinction value to de-redden the $3.6 \mu\text{m}$ flux and use it to create a column density map with our column density temperature relation. Figure 7 show the column density map of shocked H_2 in the flow. We find that there is also a correspondence between the NIR H_2 knots and regions of higher column density. Using the established distance to the RMC of 1.6 kpc and the column density map we calculate the total mass of the shocked H_2 ($T > 2000$ K) in the outflow to be 3.5×10^{30} g ($\sim 2 \times 10^{-3} M_\odot$).

3.3. Outflow Source

The source of the outflow is not seen in the NIR nor in the IRAC images. However, inspection of the MIPS $24 \mu\text{m}$ image reveals a source ($(\alpha, \delta)(J2000) = (06^{\text{h}}35^{\text{m}}25^{\text{s}}.0, +03^{\circ}56'21'')$) bisecting the outflow (Figure 8). Moreover, this source is spatially coincident with a dark patch seen in the $8 \mu\text{m}$ image. This patch is elongated nearly perpendicular to the outflow and the northwest part of it has

Table 2
IRAC color analysis of H_2 knots

Knot	T (10^3 K)	N_{H_2} (10^{18} cm^{-2})
b	2.5 ± 0.2	3.7 ± 0.3
c	2.7 ± 0.3	3.7 ± 0.2
d	2.5 ± 0.2	4.1 ± 0.2
e	2.5 ± 0.2	2.2 ± 0.2
f	2.5 ± 0.2	2.6 ± 0.2
g	3.2 ± 0.4	3.0 ± 0.1
h	3.0 ± 0.7	0.6 ± 0.1
i	3.0 ± 0.2	1.1 ± 0.1
j	3.3 ± 0.6	2.1 ± 0.1
k	2.8 ± 0.3	2.3 ± 0.2
l	3.3 ± 0.8	1.3 ± 0.1
m	2.5 ± 0.3	1.1 ± 0.2
n	2.3 ± 0.2	2.9 ± 0.4
o	2.3 ± 0.1	1.5 ± 0.3
p	2.8 ± 0.6	2.0 ± 0.2
q	2.6 ± 0.1	2.1 ± 0.2
r	4.0 ± 0.8	1.4 ± 0.1
s	2.8 ± 0.6	1.0 ± 0.2
t	2.6 ± 0.3	1.0 ± 0.2
u	3.3 ± 0.2	1.4 ± 0.1
w	2.7 ± 0.2	2.4 ± 0.2

Note. — The estimated temperature is the column density averaged temperature determined from pixel colors within each aperture. The temperature uncertainty is the column density weighted standard deviation of the temperatures corresponding to the individual pixels.

the morphology of an outflow cavity. The dark patch is seen in the contours that indicate mass surface densities obtained through extinction mapping of the $8 \mu\text{m}$ imaging data by the method of Butler & Tan (2009). The contour levels correspond to mass surface densities of $\Sigma = (2.5, 4.0, 5.0, 6.0) \times 10^{-3}$ g cm^{-2} . This small cloud may be a remnant of the core from which the protostar formed. The morphology of the northern end of the cloud appears as a bi-polar outflow cavity with an opening angle $\theta \sim 30^\circ - 40^\circ$. H_2 1–0 S(1) surface brightness contours are overlaid on the MIPS $24 \mu\text{m}$ image that bisect the MIPS source and a coincident with the cavity of the dark cloud. This source is also detected in the MIPS $70 \mu\text{m}$ and MIPS $160 \mu\text{m}$ imaging data. However, we are unable to estimate the flux in the MIPS $70 \mu\text{m}$ band image due to incomplete coverage and possible contamination from the adjacent knot (j) which may have emission from dust and the $63 \mu\text{m}$ [O I] line (Reipurth & Bally 2001). Similarly, the MIPS $160 \mu\text{m}$ band image may include emission from the knot in addition to the source. This source is not detected at shorter wavelengths and thus can be classified as a Class 0 protostar. We propose this newly discovered protostar to be the source of the outflow. Additionally, using the column density map, we find that the mass of the shocked H_2 to the east (1.8×10^{30} g) of this source is almost equal to the mass west of the source (1.7×10^{30} g).

Faint extended $24 \mu\text{m}$ emission is also detected at the locations of the brightest H_2 knots (g & j). This may arise from fine-structure [Fe II] lines within the MIPS $24 \mu\text{m}$ band (Velusamy et al. 2007). This is consistent with our IRAC color analysis of these knots that reveal them to be high temperature regions ($T \geq 3.2 \times 10^3$ K). This consistency between the IRAC color analysis and the MIP $24 \mu\text{m}$ emission validates our usage of the color space for non-dissociative shocks.

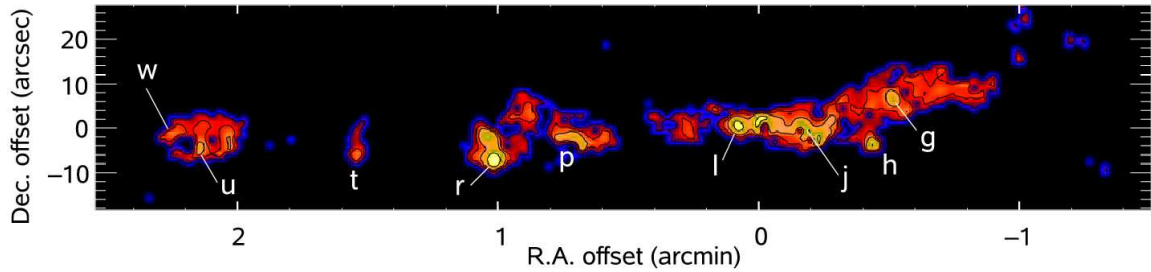


Figure 6. Thermal map of the outflow based on color analysis of the IRAC data. The contour levels indicate $T = 1500$ K, 2500 K, 3000 K, 4000 K. The origin is set at $(\alpha, \delta)(J2000) = (06^{\text{h}}35^{\text{m}}25^{\text{s}}.0, +03^{\circ}56'21'')$

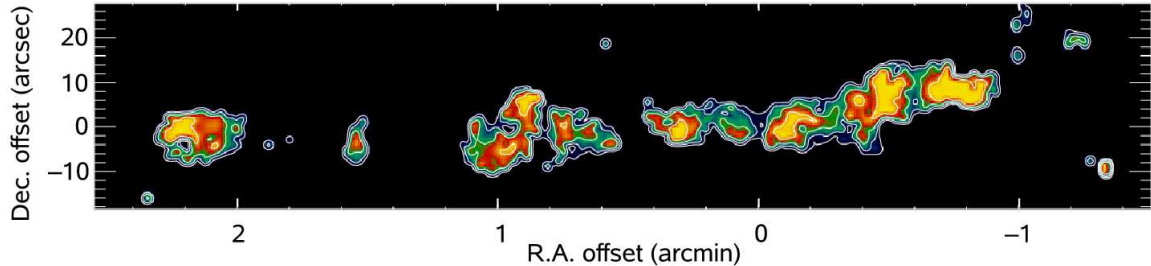


Figure 7. Column density map for H_2 of the outflow based on color analysis of the IRAC data. The contour levels indicate $N_{\text{H}_2} = 2 \times 10^{17} \text{ cm}^{-2}$, $5 \times 10^{17} \text{ cm}^{-2}$, $1 \times 10^{18} \text{ cm}^{-2}$, $2 \times 10^{18} \text{ cm}^{-2}$. The origin is set at $(\alpha, \delta)(J2000) = (06^{\text{h}}35^{\text{m}}25^{\text{s}}.0, +03^{\circ}56'21'')$

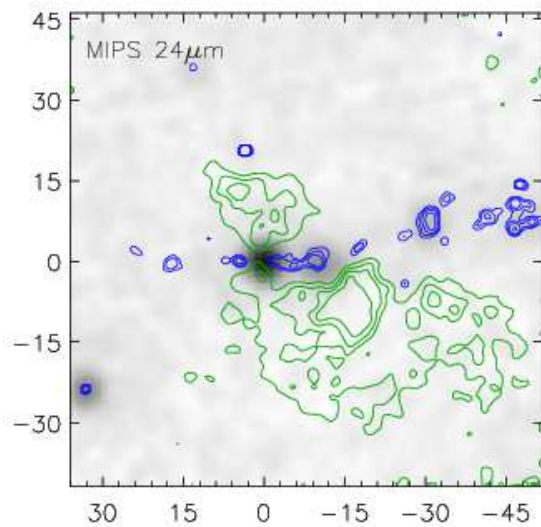


Figure 8. MIPS $24 \mu\text{m}$ image of the outflow sources. The green contours show the dark cloud that bisect the outflow and indicate the Σ values ($2.5, 4.0, 5.0,$ and 6.0) $\times 10^{-3} \text{ g cm}^{-2}$ obtained through extinction mapping using the IRAC $8 \mu\text{m}$ imaging data (Butler & Tan 2009). The blue contours are H_2 $1-0$ S(1) surface brightness contours with levels indicating $(0.5, 1.0, 2.0, 5.0)$ $\times 10^{-18} \text{ W m}^{-2} \text{ sr}^{-1}$. The H_2 contours reveal the location of the outflow. The scale of the image axes is in arcseconds. The origin is set at $(\alpha, \delta)(J2000) = (06^{\text{h}}35^{\text{m}}25^{\text{s}}.0, +03^{\circ}56'21'')$

4. DISCUSSION

4.1. Structure of the outflow

The long axis of the flow extends to $3.3'$. With a distance of 1.6 kpc to the RMC, the flow would have a projected total length of 1.5 pc. The east lobe extends $2.3'$ from the MIPS source to the bow shock, while the west lobe extends only $1'$. Assuming a projected outflow velocity of 100 km s^{-1} , using the east lobe we estimate the age of the outflow to be 10^4 years. This age is consis-

tent with the typical age of a Class 0 source and thus this outflow may provide an accretion record of the protostar (Reipurth & Bally 2001). We can estimate the mass flux of the outflow as $\dot{M} \sim M(\text{H}_2)v_t l_t$ where v_t is the projected outflow velocity and l_t is the projected outflow length. Assuming the typical value of $v_t = 100 \text{ km s}^{-1}$ and using the values for the H_2 mass and length of the east lobe, we estimate a mass flux of $\dot{M} \sim 10^{-7} M_{\odot} \text{ yr}^{-1}$. This value is consistent with those obtained from other outflows using spectroscopic data (Podio et al. 2006).

The NIR H_2 data reveals the higher temperature regions of the outflow seen in the IRAC images. The IRAC images also show the cooler regions of the flow as the IRAC bands contain pure rotational H_2 lines in addition to $\nu = 1-0$ and $\nu = 2-1$ ro-vibrational lines.

The flow is spatially coincident with two lobes of high velocity CO gas observed by Dent et al. (2009). Similar to many HH flows which extend further than their CO counterpart, we find the eastern half to extend beyond the the eastern CO lobe. The east end of the H_2 flow ends in a large bow shock, while the west end reveals a complex structure resembling either a broken up bow shock or multiple smaller bow shocks. Although the outflow is linear on large scales, the IRAC and H_2 data reveal a region in the eastern lobe before the bow shock with a more chaotic structure. This deviation from a linear progression of knots may be due to a possible interaction with another outflow. The CO observations of Dent et al. (2009) reveal another flow in the NE-SW direction originating from the embedded cluster PL07 (Phelps & Lada 1997) that points toward this region. A collision between the two flows may explain the morphology and high temperature of knot r. The distribution of knots may also be due to variations in in jet direction over time and thus an indication of jet precession.

4.2. Deflection of the Outflow

The western end of the outflow appears slightly bent northward. The outflow is deflected by an angle $\theta_d = 20^\circ$ where it appears to graze the densest region within the dark patch. The deflection angle remains small and appears to decrease slightly beyond the interaction region. This is consistent with the simulations by Baek et al. (2009) of outflows colliding with dense cloud cores where the impact parameter is large. The deflection of the outflow may explain why the western end of the flow is shorter than the eastern end as the outflow velocity is expected to decrease after the collision (Raga & Canto 1995). This is consistent with the IRAC color analysis that reveals high temperature shocked gas (knot j) to the east of the collision.

If the outflow is composed of episodic ejection of material, there may be collision between clumps of material moving through the flow due to the velocity change (Raga & Cantó 2003). As these successive clumps collide they may give rise to the high temperature and high column density region (g) found slightly west of the deflection. This interaction may also explain why the western lobe lacks the bow shock structure seen in the eastern end.

5. CONCLUSIONS

We present the discovery of a new bi-polar outflow in the Rosette Molecular Cloud and use NIR narrow-band and Spitzer imaging data to study the flow. We show that IRAC color analysis can be used to interpret the interaction of an outflow with its surrounding environment. Using our calculations of the IRAC space of non-dissociative shocked gas we fit analytic forms to the color-temperature and column density-temperature relationships. We verify that IRAC color analysis can reveal regions of shocked gas and find that the NIR H_2 knots correspond to regions of high temperature and or column density determined through color analysis. We find diffuse MIPS 24 μm emission, most likely from [Fe II] lines, to be coincident with regions of high temperature thus confirming the validity of using the non-dissociative shock IRAC color space. The NIR line ratios combined with the temperature estimates allow for the determination of extinction along the line of sight which is used to create a column density map of the shocked H_2 gas. We deduce that the asymmetry in the outflow is due to interactions with the dense material to the west of the outflow source causing deflection and possibly deceleration of the outflowing material.

We thank Mike Butler for running his extinction mapping code on the IRAC data and providing the mass surface density data shown in Figure 8. We thank the CTIO Blanco-4m observatory support scientists and staff

including Nicole van der Blik, Hernan Tirado, and Alberto Alvarez. We thank our referee, John Bally, for his useful comments and suggestions. This work is based in part on archival data obtained with the Spitzer Space Telescope, which is operated by the Jet Propulsion Laboratory, California Institute of Technology under a contract with NASA. Support for this work was provided by an award issued by JPL/Caltech and also a NASA LTSA Grant NNG05GD66G. JY acknowledges support by a Florida Space Grant Fellowship from NASA through the Florida Space Grant Consortium.

Facilities: Spitzer (IRAC,MIPS), Blanco (ISPI) .

REFERENCES

- Baek, C. H., Kim, J., & Choi, M. 2009, ApJ, 690, 944
 Bally, J. 2007, Ap&SS, 311, 15
 Butler, M. J., & Tan, J. C. 2009, ApJ, 696, 484
 Chapman, N. L., Mundy, L. G., Lai, S.-P., & Evans, N. J. 2009, ApJ, 690, 496
 Davis, C. J., Gell, R., Khanzadyan, T., Smith, M. D., & Jenness, T. 2009, arXiv:0910.5274
 Dent, W. R. F., et al. 2009, MNRAS, 395, 1805
 Draine, B. T., & Roberge, W. G. 1984, ApJ, 282, 491
 González-Alfonso, E., Wright, C. M., Cernicharo, J., Rosenthal, D., Boonman, A. M. S., & van Dishoeck, E. F. 2002, A&A, 386, 1074
 Gordon, K. D., et al. 2005, PASP, 117, 503
 Gutermuth, R. A., et al. 2008, ApJ, 674, 336
 Hollenbach, D., & McKee, C. F. 1979, ApJS, 41, 555
 Hure, J. M., & Roueff, E. 1993, Journal of Molecular Spectroscopy, 160, 335
 Indebetouw, R., et al. 2005, ApJ, 619, 931
 Le Boulrot, J., Pineau des Forêts, G., & Flower, D. R. 1999, MNRAS, 305, 802
 Le Boulrot, J., Pineau des Forêts, G., Flower, D. R., & Cabrit, S. 2002, MNRAS, 332, 985
 Micelotta, E. R., Jones, A. P., & Tielens, A. G. G. M. 2010, A&A, 510, A260000
 Phelps, R. L., & Lada, E. A. 1997, ApJ, 477, 176
 Podio, L., Bacciotti, F., Nisini, B., Eisloffel, J., Massi, F., Giannini, T., & Ray, T. P. 2006, A&A, 456, 189
 Poulton, C. J., Robitaille, T. P., Greaves, J. S., Bonnell, I. A., Williams, J. P., & Heyer, M. H. 2008, MNRAS, 384, 1249
 Raga, A. C., & Canto, J. 1995, Revista Mexicana de Astronomia y Astrofisica, 31, 51
 Raga, A. C., & Cantó, J. 2003, A&A, 412, 745
 Reipurth, B., & Bally, J. 2001, ARA&A, 39, 403
 Román-Zúñiga, C. G., Elston, R., Ferreira, B., & Lada, E. A. 2008, ApJ, 672, 861
 Secker, J. 1995, PASP, 107, 496
 Smith, H. A., Hora, J. L., Marengo, M., & Pipher, J. L. 2006, ApJ, 645, 1264
 Velusamy, T., Langer, W. D., & Marsh, K. A. 2007, ApJ, 668, L159
 Weingartner, J. C., & Draine, B. T. 2001, ApJ, 548, 296
 Wilgenbus, D., Cabrit, S., Pineau des Forêts, G., & Flower, D. R. 2000, A&A, 356, 1010
 Ybarra, J. E., & Phelps, R. L. 2004, AJ, 127, 3444
 Ybarra, J. E., & Lada, E. A. 2009, ApJ, 695, L120